Tuning a Binary Ferromagnet into a Multi-state Synapse with Spin-orbit Torque Induced Plasticity

*Yi Cao, Andrew Rushforth, Yu Sheng, Houzhi Zheng, and Kaiyou Wang**

Dr. Y. Cao, Y. Sheng, Prof. H. Zheng, Prof. K. Wang
State Key Laboratory for Superlattices and Microstructures
Institute of Semiconductors
Chinese Academy of Sciences
Beijing 100083, China
E-mail: kywang@semi.ac.cn

Prof. A. Rushforth
School of Physics and Astronomy
University of Nottingham
Nottingham NG7 2RD, United Kingdom

Prof. H. Zheng, Prof. K. Wang
Center of Materials Science and Optoelectronic Engineering
University of Chinese Academy of Science
Beijing 100049, China

Prof. K. Wang
Center for Excellence in Topological Quantum Computation
University of Chinese Academy of Science
Beijing 100049, China

* Corresponding e-mail: kywang@semi.ac.cn

Keywords: spin-orbit torques (SOTs), multi-state magnetization switching, interlayer exchange coupling, synaptic plasticity, spike timing-dependent plasticity (STDP)

Abstract

Ferromagnets with binary magnetic states are limited in applications as artificial synapses for neuromorphic computing. Here, we show how synaptic plasticity of a perpendicular ferromagnetic layer (FM1) can be obtained when it is interlayer-exchange-coupled by another in-plane ferromagnetic layer (FM2), where a magnetic-field-free current-driven multi-state magnetization switching of FM1 in the Pt/FM1/Ta/FM2 structure is induced by spin-orbit torque. We use current pulses to set the perpendicular magnetization state (represented by the anomalous Hall resistance) which acts as the synapse weight, and demonstrate spintronic implementation of the excitatory/inhibitory postsynaptic potentials and spike timing-dependent plasticity. This functionality is made possible by the action of the in-plane interlayer exchange coupling field which leads to broadened, multi-state magnetic reversal characteristics. Numerical simulations, combined with investigations of a reference sample with a single perpendicular magnetized Pt/FM1/Ta structure, reveal that the broadening is due to the in-plane field component tuning the efficiency of the spin-orbit-torque to drive domain walls across a landscape of varying pinning potentials. The conventionally binary FM1 inside our Pt/FM1/Ta/FM2 structure with inherent in-plane coupling field is therefore tuned into a multi-state perpendicular ferromagnet and represents a synaptic emulator for neuromorphic computing, paving a substantial pathway towards combination of spintronics and synaptic electronics.

1. Introduction

The source of human memory and learning lies in the plasticity of brain synapses, where the degree of connections between neurons is set by the synaptic strength (or weight), which is much more efficient than conventional computational systems in solving complex problems.[1] Inspired by this, the field of neuromorphic computing, that emulates synaptic learning functions by a single electronic device and then integrates the synaptic devices to neuron circuits, has attracted significant interest, resulting in inspirations in operating principles, algorithms and architectures.[2-4] The demonstration of synapse-like electronic devices are mainly focused on nonvolatile charge memory technologies, including field effect transistors, phase change memory, resistance change memory, ferroelectric switches, etc. These involve manipulating ions and/or electrons/holes and setting the resulting multi-state conductivity as the weight.[5-11]

In addition to the charge-based devices, devices based on the spin degree of freedom, such as magnetoelectric coupled memtranstors, spin-transfer torque (STT) memristors, and spin-orbit torque magnetic bilayers have also been suggested for implementation in synaptic electronics recently.[12-21] Stochastic synapses that utilize the intrinsic time randomness of STT reversal in a single magnetic tunnel junction (MTJ) have already shown their potential for spiking neural network (SNN) applications.[22,23] For the implementation of conventional multi-state synaptic plasticity, current-driven magnetic domain wall motion has been employed by the spintronic community.[16-19] However, since the exhibited magnetic states of a

ferromagnet are often binary, or consist of multiple states with no control over stochastic switching fields,[17] a generally applicable method that allows a binary ferromagnet to exhibit tunable multi-state current-driven switching behavior is strongly desired.

Unlike current-driven devices employing the STT, it is not necessary for the electric current to pass directly through the ferromagnetic layers in devices employing spin-orbit torques (SOTs). Therefore, current-induced magnetization switching by SOTs can have the advantages of simpler device design, and more reliable and energy efficient operation.[24] In heavy metal (HM)/ferromagnetic metal (FM) bilayer systems, the origins of the SOTs are the spin Hall effect (SHE) in the HM and/or the Rashba effect from interfacial inversion asymmetry.[25-27] When the magnetization reversal mechanism involves the nucleation and driving of domain walls by the SOTs, the presence of the Dzyaloshinskii-Moriya interaction (DMI) arising at the heavy metal/ferromagnet interface necessitates the application of a static in-plane magnetic field to realize current induced deterministic switching of perpendicular magnetization.[28] Without an external magnetic field, switching assisted by equivalent in-plane magnetic fields has been demonstrated using a wedge oxide capping layer, a polarized ferroelectric substrate, and stacks with exchange bias or interlayer exchange coupling using antiferromagnetic layers.[20,29-33] Considering that antiferromagnets have strong exchange interaction between neighboring magnetic atoms and thus small domains, spin-orbit torque induced gradual switching behaviors are observed not only in an antiferromagnet itself, but also in the neighboring

ferromagnetic layer interfaced with the antiferromagnet, respectively.[20,34] Inspired by this, Olejník et al and Borders et al respectively developed an antiferromagnetic CuMnAs multi-level memory cell, and a network consisting of 36 antiferromagnet/ferromagnet bilayer devices with magnetic-field-free multi-state SOT switching behaviors for associative memory operations, recently.[35,36] However, for a ferromagnetic system it is still challenging to experimentally control the number of magnetic switching states (from binary to multiple states) in order to enable it as a spintronic synapse.

Here, we demonstrate magnetic-field-free SOT-induced multi-state synaptic plasticity in a Pt/FM1/Ta/FM2 structure, where the layer with perpendicular magnetic anisotropy (PMA), FM1, is antiferromagnetically coupled with the layer with in-plane magnetic anisotropy (IMA), FM2. Using imaging Kerr microscopy measurements and numerical simulations, we show that the magnetization reversal proceeds via domain wall motion, with the exchange field from the top magnetic layer not only compensating the DMI-induced effective field, but also tuning the efficiency of the SOT-induced domain wall motion as a function of the strength of the pinning potential. This method of simply coupling the FM1 with the FM2 results in a range of accessible magnetic states in the FM1 and enables emulation of the synaptic functionality. Based on these spintronic devices, we demonstrate synaptic functionalities including excitatory postsynaptic potential (EPSP), inhibitory postsynaptic potential (IPSP), and spike timing-dependent plasticity (STDP), which could be important for developing neuromorphic computing.[37-39]

2. Device Preparation and Measurement Configuration

A Pt/FM1/Ta/FM2 system with stacks of Ta(0.5)/Pt(3)/Co(1.3)/Ta(1.2)/Co(4)/AlO_x(2) and a reference Pt/FM1/Ta system with stacks of Ta(0.5)/Pt(3)/Co(1.3)/Ta(1.2)/AlO_x(2) (from the substrate side, thickness in nm) were deposited on Si/SiO_2 substrates by magnetron sputtering. After deposition, the Pt/FM1/Ta/FM2 films were processed into Ta(0.5)/Pt(3) hall bars with a 6 μm-wide Co(1.3)/Ta(1.2)/Co(4)/AlO_x(2) square pillar on top of the crossing area of each Hall bar. For the Pt/FM1/Ta/FM2 system, magneto-optical Kerr characterization of the pillar shows parallelogram-shaped hysteresis loops in both out-of-plane and in-plane directions (see Supplementary Figure S1), indicating that the thinner Co(1.3 nm) layer exhibits PMA and the thicker Co(4 nm) layer exhibits IMA, which respectively serve as the free layer and the fixed layer. The Pt/FM1/Ta reference system was processed into the same device configuration, i.e. Ta(0.5)/Pt(3) Hall bars, but with a 6 μm-wide (and also a 20 μm-wide) Co(1.3)/Ta(1.2)/AlO_x(2) square pillar at the cross of each Hall bar.

Measurements of both the magneto-optic Kerr effect and the Hall resistance (R_H) from the anomalous Hall effect (AHE) were used to evaluate the perpendicular magnetization component (m_z) of the Co(1.3 nm) free layer in the pillars. As shown in **Figure 1a**, the input currents for the AHE measurement and for the SOT-induced switching were applied along the *x*-direction, while the AHE voltage (V_H) was detected at the other channel with +*y*-direction. R_H was obtained by dividing V_H with a low measurement d.c. current of 100 μA. Note that with this measurement geometry,

the sign of R_H is in accordance with the direction of m_z, i.e. positive (negative) R_H represents +z (-z) directed moment. The current pulse densities in this article are calculated from the pulse intensities divided by the whole thicknesses of the conducting stacks for simplicity.

3. Demonstration of Spintronic EPSP/IPSP and STDP

We characterize the Pt/FM1/Ta/FM2 device by examining its R_H-$\mu_0 H_z$ loops as a function of maximum applied magnetic field $\mu_0 H_z^{max}$. Prior to the measurements, a 20 mT external magnetic field was used to pre-magnetize the magnetization of the in-plane Co(4 nm) layer along the +x-direction. Then, the in-plane magnetic field was removed. **Figure 1b** shows the R_H-$\mu_0 H_z$ loops measured with the perpendicular field scanning from -11.7 mT to several different $\mu_0 H_z^{max}$, and then back to -11.7 mT, where the $\mu_0 H_z^{max}$ varies from smaller to larger than the saturation field ($\mu_0 H_z^{s}$, around 7 mT). Instead of showing binary states, the loops enlarge gradually with the increasing $\mu_0 H_z^{max}$ before it reaches the saturation field, indicating controllable magnetization reversal processes in our structure. Next, we investigate the response of R_H to J_x under zero magnetic field, where the in-plane Co(4 nm) fixed layer is expected to provide an assisting field for SOT-induced switching of the perpendicular Co(1.3 nm) free layer.[40] After setting the device to a negative maximum R_H state, we applied a sequence of 10 ms-long pulses with scanning magnitude from -16.67×10^{10} A m^{-2} to 16.67×10^{10} A m^{-2} and then back to -16.67×10^{10} A m^{-2}. A low d.c. current of 100 μA was used to monitor R_H after each pulse, and the measured R_H-J_x loop is plotted in

Figure 2c. A change in R_H with J_x is observed as expected, indicating that the perpendicular magnetization in the Co(1.3 nm) free layer is reversed solely by the current-induced torque. The threshold switching current density (J_x^{th}) and the finishing switching current density (J_x^{f}) are defined as the absolute values of J_x at which the change of R_H begins and finishes, which is around 7×10^{10} A m^{-2} and 16.67×10^{10} A m^{-2} for current applied along +*x*-direction in **Figure 2c**. We have also measured the R_H-J_x loop with scanning range of $\pm18.33\times10^{10}$ A m^{-2} to confirm that $\pm16.67\times10^{10}$ A m^{-2} is sufficient to fully switch the R_H to its maximum current-driven switchable values without bringing potential thermal perturbation to the switching loop. The different magnitudes of the changes in R_H for the Hall measurement in **Figure 1b** and the field-free SOT-induced switching measurement in **Figure 1c** are ascribed to the unsaturated remanence of the in-plane FM2 layer in the latter case (see Supplementary Note 1 for detail). Similar to the R_H-μ_0H_z loops, the R_H-J_x loop also exhibits a gradual reversal behavior, showing that the multiple perpendicular magnetic states in our device can be obtained through current-induced switching. The intermediate magnetization states are nonvolatile within our measurement time scale after an initial small relaxation, as shown by the R_H-*time* relations in Supplementary Note 2. The sense of rotation of the R_H-J_x loop is reversed if FM2 is pre-magnetized along the -*x*-direction (see Supplementary Note 3). This flexible feature of adjustable current-induced switching directions in our multi-state magnetic system will bring additional functionalities when combined with the synaptic implementations discussed below. The anticlockwise and clockwise sense of field free current-induced

magnetization switching with pre-magnetization of the top FM2 layer along the +x and -x directions respectively, suggests that there is in-plane antiferromagnetic coupling between FM1 and FM2.[40,41] The type of this antiferromagnetic coupling is confirmed to be the Ruderman-Kittel-Kasuya-Yosida (RKKY) interlayer exchange coupling after excluding the possibility of the ferromagnetic Néel orange peel coupling and the very small (<<1mT for our stacks with 6 μm-wide pillar) antiferromagnetic magneto-static coupling.[42,43] The magnitude of this antiferromagnetic interlayer exchange coupling field ($\mu_0 H_x^c$) is at an optimum value of around -180 mT for our multilayer stacks, as illustrated by the R_H-J_x characteristics under various magnetic fields along the +x-direction ($\mu_0 H_x$) (see Supplementary Note 4).

This multi-magnetic-state switching behavior under current pulses can be analogous to the information transmission characteristics of biological synapses. A synapse is a conjunction of two neuron cells, named pre-neuron and post-neuron. Under an external stimulus, spikes or action potentials from the pre-neuron are transmitted through the synapse to the post-neuron and generate excitatory postsynaptic potentials (EPSP) or inhibitory postsynaptic potentials (IPSP), together with synaptic weight updates.[37] Here, the artificial synapse characteristics based on our Pt/FM1/Ta/FM2 structure can be achieved by regarding the perpendicular magnetization component, m_z as the synaptic weight. The applied current pulses play the roles of the pre- and post-spikes that act on our artificial synapse to modulate m_z, which is assessed by the detection of R_H. Therefore, the increasing and decreasing of

R_H, as shown in **Figure 1c**, indicates the synaptic plasticity of EPSP and IPSP, respectively. In addition to the pulse magnitude-induced EPSP/IPSP, we also examined the effect of pulse numbers on the switching of R_H at different fixed pulse magnitudes. As shown in **Figure 1d**, sequences of 50 pulses with constant magnitude (J_x) and duration of 10 ms are applied to the channel, and R_H is measured 2 seconds after each pulse. Before the application of each sequence, an initialization pulse with magnitude of -16.67×10^{10} A m^{-2} was applied to align the magnetization in the -z-direction. With increasing pulse number, R_H initially increases quickly and then gradually reaches a relatively stable value for J_x ranging from 8.33×10^{10} A m^{-2} to 13.33×10^{10} A m^{-2}, where the stable value increases as a function of the pulse magnitude. For J_x = 15×10^{10} A m^{-2}, R_H jumps directly from the minimum to approximately the maximum value by the first pulse, which is because the applied pulse is close to J_x^f. By applying a sequence of 6 alternating pulse strings (20 pulses per string) with moderate J_x of 11.67×10^{10} A m^{-2} and -12.5×10^{10} A m^{-2}, consecutive EPSPs and IPSPs are induced only by pulse numbers, as shown by the patterns of multiple increasing and decreasing R_H values in **Figure 1e**. Since sequences with identical pulses required simpler circuit design than those with varying magnitude, the EPSP/IPSPs used in **Figure 1e** will be more practical to implement in neural network systems than the EPSP/IPSPs shown in **Figure 1c**.[12]

Figure 2a illustrates STDP. A long-term depression (LTD) or long-term potentiation (LTP) of the synaptic weight occurs when the post-neuron spikes just before ($\Delta t < 0$) or after ($\Delta t > 0$) the pre-neuron spikes, respectively, where the typical

STDP window of a biological synapse can be found in Figure 7 of Ref. 38.[38] It is also characterized by the $|\Delta t|$ dependence of the synaptic potentiation/depression magnitudes, i.e. closer spikes bring stronger stimulation. A biological synapse realizes such plastic functions by regulating the ion concentrations inside it,[44] whereas a spintronic synapse may adopt the changes in magnetic state during the current controlled switching process as an analogue. The existence of separate J_x^{th} and J_x^f makes it possible to implement STDP in our device. Changes in R_H induced by single current pulses, as a function of the pulse magnitude J_x are shown in **Figure 2b**. Before the application of each single pulse, the sample was reset to an almost zero m_z state ($R_H \approx 0$). For $J_x > J_x^{th}$ or $-J_x > -J_x^{th}$, an increase or a decrease of R_H can be induced by the single pulse, and higher $|J_x|$ brings greater change in R_H until $|J_x|$ approaches $|J_x^f|$ (note that $|J_x^f|$ for single pulse here is slightly larger than that for consecutive pulses in **Figure 1c**). Based on this J_x dependence of R_H under single current pulse, spikes as shown in **Figure 2c** are designed for the demonstration of STDP in our device. The pre-spike and post-spike share the same waveform but are opposite in polarity. In this way, although the current density of a single pre- or post-spike never exceeds J_x^{th}, the overlapped waveform will produce a short over threshold peak, whose sign and magnitude depend on the Δt. Results of the pre-and post-spikes acting on the channel of our device with $R_H \approx 0$ are shown in **Figure 2d**, where a field-free SOT-induced STDP window is obtained. The distribution of the weakened (LTD, when $\Delta t < 0$) and the strengthened (LTP, when $\Delta t > 0$) Hall resistances show decent fidelity with two nearly linear R_H-Δt responses in the first and the third quadrants, as well as tolerable

R_H deviations for repeated measurements. The form of a STDP window is important because different STDP forms can emulate different types of neuron activities that vary significantly according to the location of the synapses in a brain, and the outcome of a certain learning procedure in a spike neural network is highly dependent on the STDP form of an artificial synapse.[6,11] In **Figure 2e**, we then modified the spike shapes with two adjusted decay slopes and obtained corresponding STDP windows with distinct forms, as shown in **Figure 2f**. This further illustrates that the demonstrated spintronic synapse could be practically used for spike-based neuromorphic computing applications with the capability of implementing versatile STDP forms, including the exponential STDP form,[45] via simply modulating the spike shapes (see the simulations in Supplementary Note 5 for detail).

4. Correlation between Multi-state m_z and $\mu_0 H_x$

To understand the origin of the multi-state magnetization reversal of FM1 in the Pt/FM1/Ta/FM2 system, we will focus on a Pt/FM1/Ta reference system without the FM2 layer. The measured R_H-H_z loop for the Hall bar with 6 μm-wide square pillar, shown in **Figure 3b**, exhibits perfect rectangularity, representing binary m_z states in the Pt/FM1/Ta reference structure with good PMA. This is distinct from the multi-state magnetization reversal observed in the Pt/FM1/Ta/FM2 system. Without an in-plane external magnetic field applied, no deterministic current-induced magnetization switching is observed. With a small external in-plane magnetic field, $\mu_0 H_x$ = 20 mT, applied in the +x-direction, a very sharp current pulse induced

clockwise R_H-J_x loop is observed (**Figure 3c**). Interestingly, with increasing the external magnetic field from 40 mT to 240 mT, the R_H-J_x loops, as shown in **figure 3d** become more parallelogram-like. The dependence of J_x^{th} and J_x^f on $\mu_0 H_x$ are plotted in **Figure 4e**. J_x^{th} decreases continually with increasing $\mu_0 H_x$, while the variation of J_x^f does not obey the J_x^{th}-H_x trend well, instead showing a relatively slowly decreasing J_x^{th}-H_x relationship as $\mu_0 H_x$ increases from 40 mT to 100 mT, an increasing J_x^{th}-H_x dependence when $\mu_0 H_x$ ranges from 100 mT to 180 mT, and a decreasing J_x^{th}-H_x relation again for $\mu_0 H_x$ larger than 180 mT. As a consequence, an increasingly current-controllable region (defined as $\Delta J_x = J_x^{th} - J_x^f$) with the growing $\mu_0 H_x$ is obtained, as shown in **Figure 3f**. To quantify the degree of the current control of the multiple magnetic states, we introduce $\Delta J_x/J_x^f$ to describe the fraction of current-controllable region during the applied current pulse rising from zero to J_x^f. As shown in **Figure 3f**, peaks in ΔJ_x and $\Delta J_x/J_x^f$ correspond with $\mu_0 H_x$ around 180 mT and 200 mT, suggesting our Ta(0.5)/Pt(3)/Co(1.3)/Ta(1.2)/Co(4)/AlO_x(2) system with built-in $\mu_0 H_x^c \approx$ -180 mT is the optimized structure for synaptic emulation in terms of the availability of multiple magnetization states. In the Supplementary Note 6 we present numerical calculations which reveal that the increase of ΔJ_x with $\mu_0 H_x$ arises from the tuning of the efficiency of the SOT to drive domain wall motion in a pinning potential by $\mu_0 H_x$, where the pinning potential can strongly affect the velocity of domain wall motion. In addition, $\mu_0 H_x$ tilts m_z within the up/down domains, leading to a reduction in the maximum values of R_H (R_H^{max}). **Figure 3g** shows R_H^{max} as a function of $\mu_0 H_x$. An external field with $\mu_0 H_x >$ 200 mT causes overwhelming loss of

PMA, and coincides with the drop of ΔJ_x and $\Delta J_x/J_x^f$, resulting in a loss of accessible magnetic states.

In this way, we have successfully tuned an originally binary perpendicular ferromagnet FM1 into a multi-state one by simply coupling it with another in-plane ferromagnet FM2 via a normal metal spacer layer (in our case, Ta). The particular m_z among the multiple perpendicular magnetic states of the FM1 inside our Pt/FM1/Ta/FM2 structure can be controlled by spin-orbit torque induced current-driven magnetic switching without assistance of any external magnetic field, making it capable of performing synaptic plasticity of EPSP, IPSP, and STDP. Note that the magnitude of the RKKY interlayer exchange coupling field can be manipulated by a fully electrical method such as ionic liquid gating, which would effectively change the functions of R_H versus single pulse's J_x in **Figure 2b**.[46,47] Accordingly, our Pt/FM1/Ta/FM2 synapses have potential novel advantages with versatile electrically controllable plasticity forms, such as variable STDP windows, the form of which can be modulated not only by altering the spike waveforms, but also potentially by electrically controlling the interlayer exchange couplings. This diversity in controllable STDP windows would serve for specific computing at different stages of the neuromorphic pathway (see the simulations in Supplementary Note 7 for detail).[45,48] Considering that the Ta spacer layer alone could also act as a spin current generator for SOT-induced switching,[49] the demonstrated multi-state PMA/IMA interlayer exchange coupled structure in this work has flexibility to be extended to MTJ stacks, which will give acceptable tunneling magnetoresistance

(TMR) ratios for cascading operations. The device is also capable of miniaturization towards the scale of the domain wall (which is of the order of 10 nm), since SOT-induced switching in magnetic layers with dimensions larger than that are governed by nucleation and domain wall motion.[28,32,50]

5. Conclusions

In conclusion, we have tuned a binary perpendicular ferromagnet FM1 into a multi-state spintronic Pt/FM1/Ta/FM2 artificial synapse that functions primarily on the basis of field-free spin-orbit torque driven domain wall motion in the FM1 layer with inherent in-plane interlayer exchange coupling from the FM2 layer. The multi-magnetic-state feature of FM1 is confirmed to be dependent on the in-plane coupling field. The ability to set multiple magnetic states, depending on the pulse number and magnitude enables spintronic implementations of plastic functionalities including EPSP, IPSP, and STDP. Our results suggest a practical way towards spintronic synaptic emulation using current controlled multi-state perpendicular magnetic materials with built-in equivalent in-plane magnetic fields, as artificial synapses for neuromorphic computing.

Experimental Section

Film Preparation: The films were deposited at room temperature onto Si wafers with a natural oxidation layer. Radio-frequency (RF) magnetron sputtering was used to

deposit the AlO_x layer, and d.c. magnetron sputtering was used to deposit the other layers. The base pressure of the chamber was less than 2×10^{-6} Pa, and Ar gas was used for sputtering. The pressure of the chamber is 1.067×10^{-1} Pa during deposition. No magnetic field was applied during the sputtering. The deposition rates for Ta, Pt, Co, AlO_x layers were controlled to be ≈0.0139 nm s^{-1}, 0.0194 nm s^{-1}, 0.0093 nm s^{-1}, and 0.0016 nm s^{-1}, respectively.

Device Fabrication: The deposited films were processed into Hall devices by two steps of standard electron-beam lithography (EBL) and Ar ion etching. First, the film was patterned into a cross shape Hall bar. Then, the central square area of the cross was patterned into a pillar, leaving the rest of the Hall bar with only stacks of Ta(0.5 nm)/Pt(3 nm).

Characterization and Measurement: The Kerr characterization of the magnetization hysteresis and domain patterns was taken using a NanoMoke3 magneto-optical Kerr microscopy. The anomalous Hall effect measurements were carried out at room temperature with Keithley 2602B as the current source and Keithley 2182 as the nanovoltmeter. The input spikes for STDP measurement as shown in **Figure 2c** and **Figure 2e** were generated using an Agilent B1500A semiconductor device analyzer with the semiconductor pulse generator unit (SPGU).

Supporting Information

Supplementary Information is available from the Wiley Online Library or from the authors.

Acknowledgements

This work was supported by National Key R&D Program of China No.2017YFA0303400 and 2017YFB0405700. This work was supported also by the NSFC Grant No. 11474272, and 61774144. The Project was sponsored by Chinese Academy of Sciences, grant No. QYZDY-SSW-JSC020, XDB28000000 and XDPB12 as well.

Competing Interests

The authors declare no competing financial interests.

Additional Information

Correspondence and requests for materials should be addressed to K.W.

References

1. L. F. Abbott, S. B. Nelson, *Nat. Neurosci*. **2000**, *3*, 1178.
2. D. Kuzum, S. Yu, H. S. Wong, *Nanotechnology* **2013**, *24*, 382001.
3. M. Prezioso, F. Merrikh-Bayat, B. D. Hoskins, G. C. Adam, K. K. Likharev, D. B. Strukov, *Nature* **2015**, *521*, 61.
4. M. A. Zidan, J. P. Strachan, W. D. Lu, *Nat. Electron.* **2018**, *1*, 22.
5. C. S. Yang, D. S. Shang, N. Liu, G. Shi, X. Shen, R. C. Yu, Y. Q. Li, Y. Sun, *Adv. Mater.* **2017**, *29*, 1700906.
6. D. Kuzum, R. G. D. Jeyasingh, B. Lee, H. S. Wong, *Nano Lett.* **2011**, *12*, 2179.
7. S. H. Jo, T. Chang, I. Ebong, B. B. Bhadviya, P. Mazumder, W. Lu, *Nano Lett.* **2010**, *10*, 1297.

8. Z. Wang, S. Joshi, S. E. Savel'ev, H. Jiang, R. Midya, P. Lin, M. Hu, N. Ge, J. P. Strachan, Z. Li, Q. Wu, M. Barnell, G. Li, H. L. Xin, R. S. Williams, Q. Xia, J. J. Yang, *Nat. Mater.* **2016**, *16*, 101.
9. S. Choi, S. H. Tan, Z. Li, Y. Kim, C. Choi, P. Chen, H. Yeon, S. Yu, J. Kim, *Nat. Mater.* **2018**, *17*, 335.
10. Y. Shi, X. Liang, B. Yuan, V. Chen, H. Li, F. Hui, Z. Yu, F. Yuan, E. Pop, H. P. Wang, M. Lanza, *Nat. Electron.* **2018**, *1*, 458.
11. S. Boyn, J. Grollier, G. Lecerf, B. Xu, N. Locatelli, S. Fusil, S. Girod, C. Carrétéro, K. Garcia, S. Xavier, J. Tomas, L. Bellaiche, M. Bibes, A. Barthélémy, S. Saïghi, V. Garcia, *Nat. Commun.* **2017**, *8*, 14736.
12. J. X. Shen, D. S. Shang, Y. S. Chai, S. G. Wang, B. G. Shen, Y. Sun, *Adv. Mater.* **2018**, *30*, 1706717.
13. N. Locatelli, V. Cros, J. Grollier, *Nat. Mater.* **2014**, *13*, 11.
14. A. Fernández-Pacheco, R. Streubel, O. Fruchart, R. Hertel, P. Fischer, R. P. Cowburn, *Nat. Commun.* **2017**, *8*, 15756.
15. A. Sengupta, K. Roy, *Phys. Rev. Appl.* **2016**, *5*, 024012.
16. P. Krzysteczko, J. Münchenberger, M. Schäfers, G. Reiss, A. Thomas, *Adv. Mater.* **2012**, *24*, 762.
17. S. Lequeux, J. Sampaio, V. Cros, K. Yakushiji, A. Fukushima, R. Matsumoto, H. Kubota, S. Yuasa, J. Grollier, *Sci. Rep.* **2016**, *6*, 31510.
18. A. Sengupta, Z. A. Azim, X. Fong, K. Roy, *Appl. Phys. Lett.* **2015**, *106*, 10464.
19. A. Sengupta, A. Banerjee, K. Roy, *Phys. Rev. Appl.* **2015**, *6*, 064003.
20. S. Fukami, C. Zhang, S. DuttaGupta, A. Kurenkov, H. Ohno, *Nat. Mater.* **2016**, *15*, 535.
21. J. M. Lee, K. Cai, G. Yang, Y. Liu, R. Ramaswamy, P. He, H. Yang, *Nano Lett.*

2018, *18*, 4669.

22. A. F. Vincent, J. Larroque, N. Locatelli, N. B. Romdhane, O. Bichler, C.Gamrat, W. S. Zhao, J. Klein, S. Galdin-Retailleau, D. Querlioz, *IEEE Trans. Biomed. Circuits Syst.* **2015**, *9*, 166.
23. G. Srinivasan, A. Sengupta, K. Roy, *Sci. Rep.* **2016**, *6*, 29545.
24. A. Brataas, K. M. D. Hals, *Nat. Nanotech.* **2014**, *9*, 86.
25. L. Liu, O. J. Lee, T. J. Gudmundsen, D. C. Ralph, R. A. Buhrman, *Phys. Rev. Lett.* **2012**, *109*, 96602.
26. L, Liu, C. F. Pai, Y. Li, H. W. Tseng, D. C. Ralph, R. A. Buhrman, *Science* **2012**, *336*, 555.
27. I. M. Miron, K. Garello, G. Gaudin, P. Zermatten, M. V. Costache, S. Auffret, S. Bandiera, B. Rodmacq, A. Schuhl, P. Gambardella, *Nature* **2011**, *476*, 189.
28. A. Thiaville, S. Rohart, É. Jué, V. Cros, A. Fert, *Europhys. Lett.* **2012**, *100*, 57002.
29. G. Yu, P. Upadhyaya, Y. Fan, J. G. Alzate, W. Jiang, K. L. Wong, S. Takei, S. A. Bender, L. Chang, Y. Jiang, M. Lang, J. Tang, Y. Wang, Y. Tserkovnyak, P. K. Amiri, K. L. Wang, *Nat. Nanotech.* **2014**, *9*, 548.
30. K. Cai, M. Yang, H. Ju, S. Wang, Y. Ji, B. Li, K. W. Edmonds, Y. Sheng, B. Zhang, N. Zhang, S. Liu, H. Zheng, K. Wang, *Nat. Mater.* **2017**, *16*, 712.
31. Y. W. Oh, S. C. Baek, Y. M. Kim, H. Y. Lee, K. D. Lee, C. G. Yang, E.S. Park, K. S. Lee, K. W. Kim, G. Go, J. R. Jeong, B. C. Min, H. W. Lee, K. J. Lee, B. G. Park, *Nat. Nanotech.* **2016**, *11*, 878.
32. Y. C. Lau, D. Betto, K. Rode, J. M. Coey, P. Stamenov, *Nat. Nanotech.* **2016**, *11*, 758.
33. W. Y. Kwak, J. H. Kwon, P. Grünberg, S. H. Han, B. K. Cho, *Sci. Rep.* **2018**, *8*,

3826.

34. P. Wadley, B. Howells, J. Železný, C. Andrews, V. Hills, R. P. Campion, V. Novák, K. Olejník, F. Maccherozzi, S. S. Dhesi, S. Y. Martin, T. Wagner, J. Wunderlich, F. Freimuth, Y. Mokrousov, J. Kuneš, J. S. Chauhan, M. J. Grzybowski, A. W. Rushforth, K. W. Edmonds, B. L. Gallagher, T. Jungwirth, *Science* **2016**, *351*, 587.
35. K. Olejník, V. Schuler, X. Martí, V. Novák, Z. Kašpar, P. Wadley, R. P. Campion, K. W. Edmonds, B. L. Gallagher, J. Garces, M. Baumgartner, P. Gambardella, T. Jungwirth, *Nat. Commun.* **2017**, *8*, 15434.
36. W. A. Borders, H. Akima, S. Fukami, S. Moriya, S. Kurihara, Y. Horio, S. Sato, H. Ohno, *Appl. Phys. Express* **2017**, *10*, 013007.
37. H. Markram, J. Lübke, M. Frotscher, B. Sakmann, *Science* **1997**, *275*, 213.
38. G. Q. Bi, M. M. Poo, *J. Neurosci.* **1998**, *18*, 10464.
39. C. Zamarreño-Ramos, L. A. Camuñas-Mesa, J. A. Pérez-Carrasco, T. Masquelier, T. Serrano-Gotarredona, B. Linares-Barranco, *Front. Neurosci.* **2011**, *5*, 26.
40. Y. Sheng, K. W. Edmonds, X. Ma, H. Zheng, K. Wang, *Adv. Electron. Mater.* **2018**, *4*, 180224.
41. K. Garello, I. M. Miron, C. O. Avci, F. Freimuth, Y. Mokrousov, S. Blügel, S. Auffret, O. Boulle, G. Gaudin, P. Gambardella, *Nat. Nanotech.* **2013**, *8*, 587.
42. L. Néel, *Ann. Phy.* **1967**, *2*, 61.
43. K. S. Moon, R. E. Fontana Jr., S. S. P. Parkin, *Appl. Phys. Lett.* **1999**, *74*, 3690.
44. R. D. Burgoyne, *Nat. Rev. Neurosci.* **2007**, *8*, 182.
45. G. Q. Bi, M. M. Poo, *Annu. Rev. Neurosci.* **2001**, *24*, 139.
46. Q. Yang, L. Wang, Z. Zhou, L. Wang, Y. Zhang, S. Zhao, G. Dong, Y. Cheng, T. Min, Z. Hu, W. Chen, K. Xia, M. Liu, *Nat. Commun.* **2018**, *9*, 991.

47. Q. Yang, Z. Zhou, L. Wang, H. Zhang, Y. Cheng, Z. Hu, B. Peng, M. Liu, *Adv. Mater.* **2018**, *30*, 1800449.

48. A. Saudargiene, B. Porr, F. Wörgötter, *Neural Computation* **2004**, *16*, 595.

49. S. Woo, M. Mann, A. J. Tan, L. Caretta, G. S. D. Beach, *Appl. Phys. Lett.* **2014**, *105*, 212404.

50. P. P. J. Haazen, E. Murè, J. H. Franken, R. Lavrijsen, H. J. M. Swagten, B. Koopmans, *Nat. Mater.* **2013**, *12*, 299.

Figures and Figure Captions

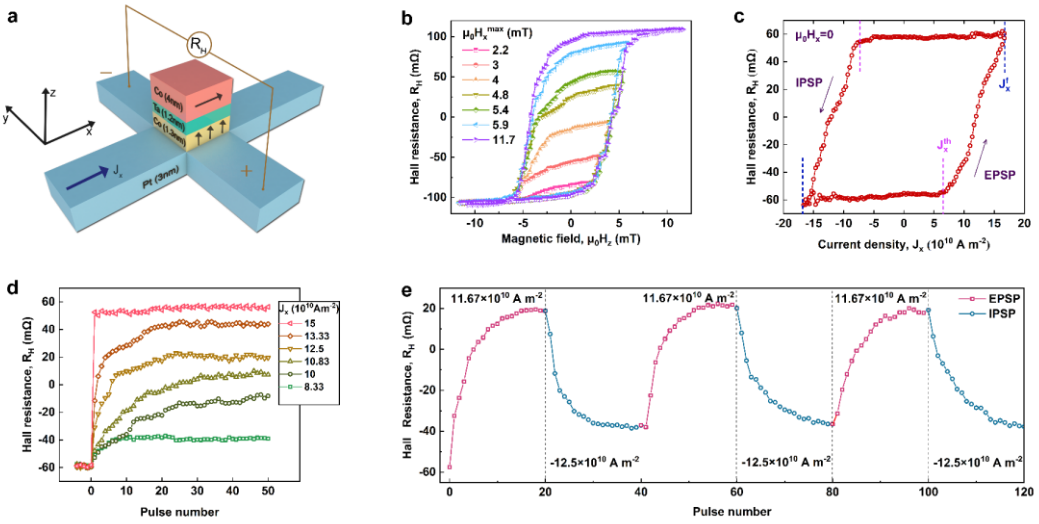

Figure 1 Device structure, magnetic switching properties, and excitatory/inhibitory synaptic behaviors. a, Schematic of the Pt/FM1/Ta/FM2 double magnetic layered system and the AHE/SOT measurement configuration with definition of x-y-z coordinates. The device consists of a Ta(0.5 nm)/Pt(3 nm) Hall bar with a 6 μm-wide Co(1.3 nm)/Ta(1.2 nm)/Co(4 nm)/AlO_x(2 nm) square pillar at the cross, where the FM1 Co(1.3 nm) layer and the FM2 Co(4 nm) layer exhibit PMA and IMA, respectively. The magnetization of the FM2 Co(4 nm) layer is pre-magnetized along the +*x*-direction. **b,** R_H-H_z loops with $\mu_0 H_z$ scanning

from -11.7 mT to $\mu_0 H_z^{max}$ and then back to -11.7 mT. **c,** The R_H-J_x loop with no external field. A sequence of pulses with scanning magnitude from -16.67×10^{10} A m^{-2} to 16.67×10^{10} A m^{-2} and then back to -16.67×10^{10} A m^{-2} is applied. The J_x^{th} and the J_x^f denote the threshold and the finishing current densities for the SOT-induced switching, respectively. **d,** R_H as a function of the pulse number for sequences of pulses with constant magnitude J_x. **e,** Evolution of the EPSP/IPSP (i.e. R_H) by applying a sequence of pulse strings with magnitude of 11.67×10^{10} A m^{-2} and -12.5×10^{10} A m^{-2}. Before apply each sequence of pulses for **d** and **e**, an initialization pulse with a magnitude of -16.67×10^{10} A m^{-2} is applied to the channel. The duration of every pulse is 10 ms, and every R_H is measured 2 seconds after the application of each pulse. For the AHE detection of R_H in **b-e**, a small $+x$ directed d.c. current with fixed magnitude of 100 μA is used as the current source. μ_0 is permeability in the free space.

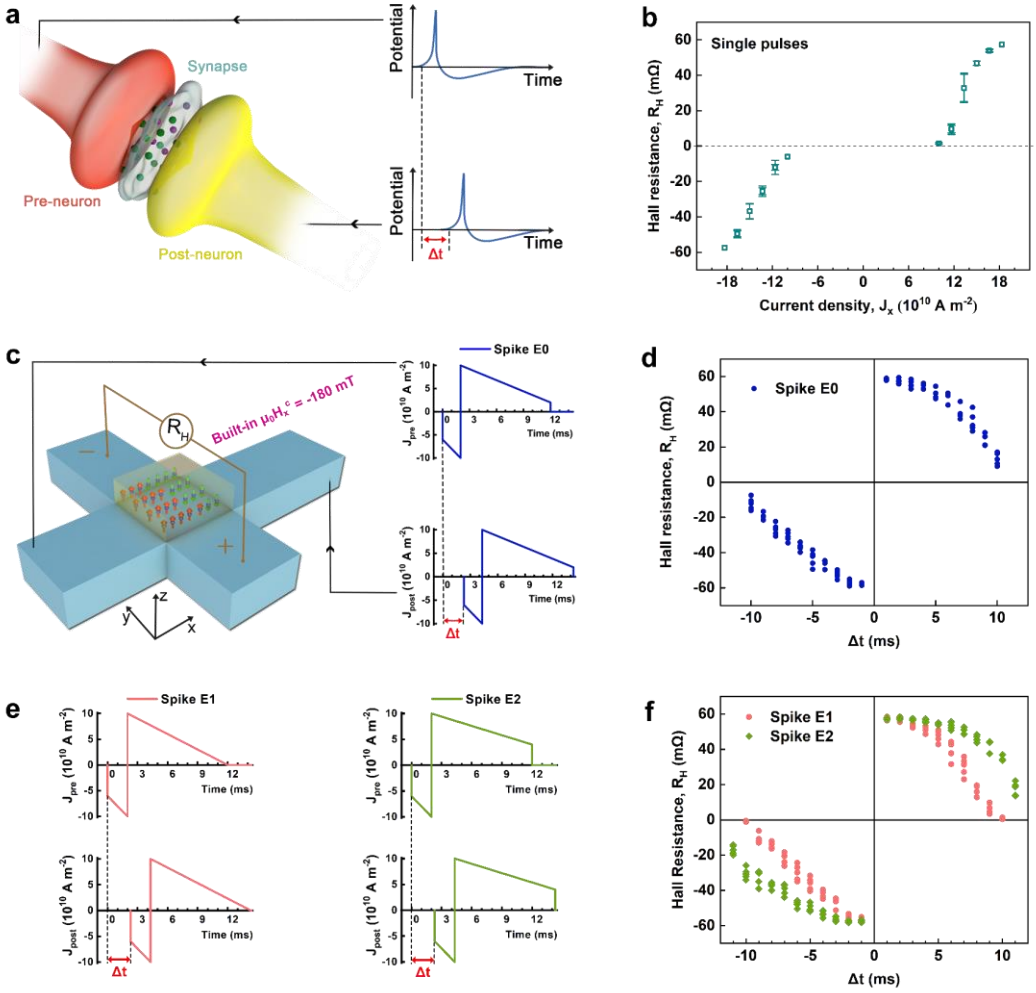

Figure 2 Field-free SOT-induced STDP in Pt/FM1/Ta/FM2 system. a, Sketch of a biological synapse sandwiched between pre- and post-neurons, where the synaptic transmission is modulated by the causality (Δt) of neuron stimuli which controls the ion channels. **b,** R_H as a function of J_x for the Pt/FM1/Ta/FM2 device (initialized in the $R_H \approx 0$ state) when only one current pulse with duration of 1 ms is applied. **c,** Sketch of our Pt/FM1/Ta/FM2 artificial synapse. The m_z (i.e. R_H) is modulated by the causality (Δt) of the engineered spikes (named Spike E0) from both ends of the x channel. **d,** STDP window (i.e. the R_H-Δt distribution) with the spikes shown in **c** (blue spike curves). **e,** another two spikes with different decay slopes named Spike E1 (pink spike curves) and Spike E2 (green spike curves). **f,** STDP window generated with spikes E1 and E2. Before the application of every

single pulse or mixed spike in **b**, **d**, and **f**, the sample is switched to an almost zero m_z state with $R_H \approx 0$. The AHE measurement with a small $+x$ directed d.c. current source of 100 μA is taken more than 2 seconds after the singe pulse or mixed spike ends. This procedure (set $R_H \approx 0 \rightarrow$ apply pulse/spike $\rightarrow$ measure $R_H \rightarrow$ set $R_H \approx 0$) repeats at least five times for each J_x or Δt. The spread of R_H data points is represented in the forms of error bars (in **b**) and scatter diagrams (in **d** and **f**), respectively.

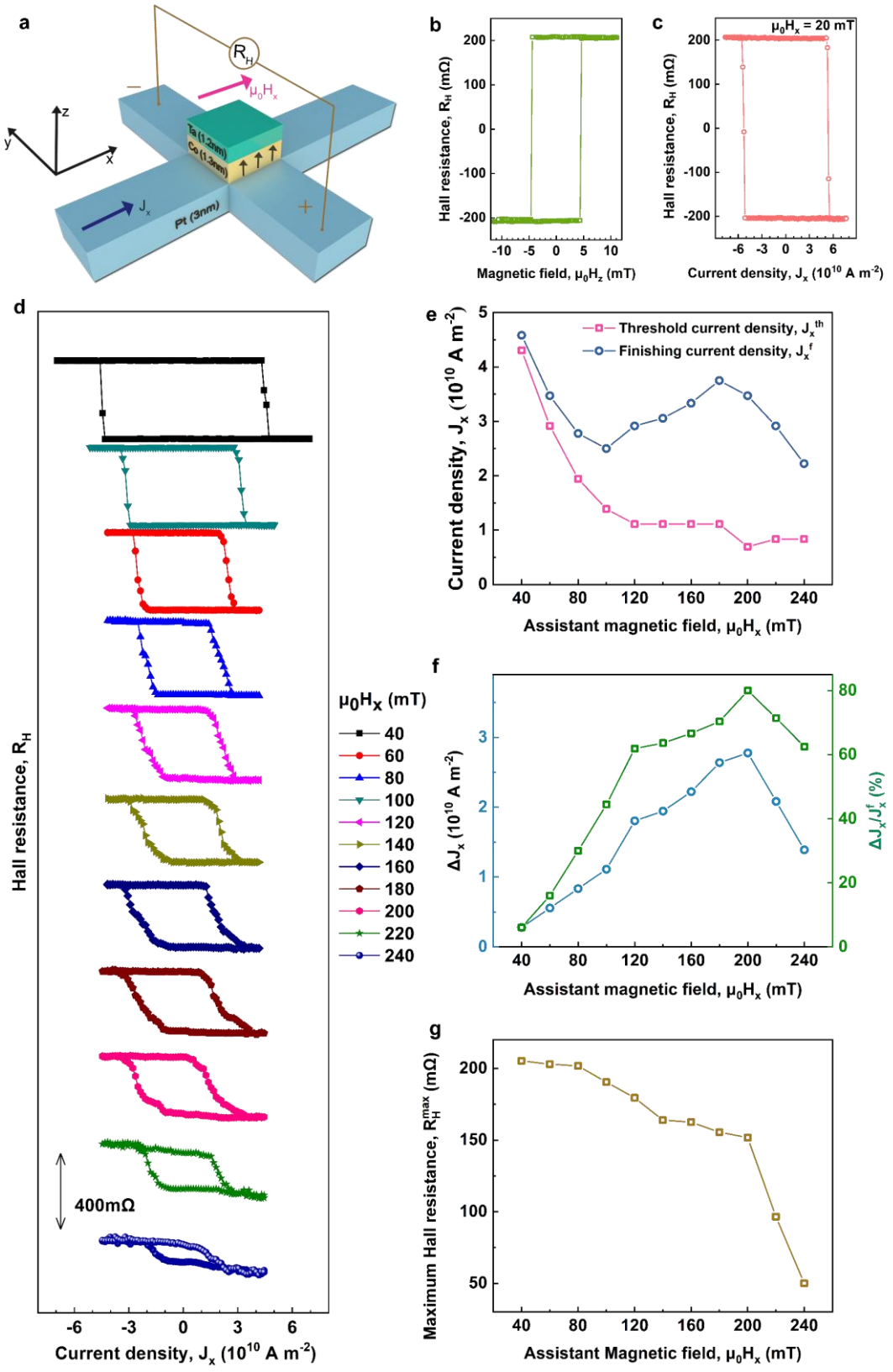

Figure 3 SOT switching of Pt/FM1/Ta reference sample. a, schematic of the Pt/FM1/Ta reference device that consists of a Ta(0.5 nm)/Pt(3 nm) Hall bar with a 6 μm-wide Co(1.3

nm)/Ta(1.2 nm)/AlO_x(2 nm) square pillar at the cross. During the measurements, an external assistant magnetic field $\mu_0 H_x$ is applied along the +*x*-direction. **b,** R_H-$\mu_0 H_z$ loop with $\mu_0 H_x$ = 0. **c,** Pulse current-driven R_H-J_x SOT switching loop with $\mu_0 H_x$ = 20 mT. **d,** Pulse current-driven R_H-J_x SOT switching loops with various $\mu_0 H_x$ from 40 mT to 240 mT. Loops are shifted vertically for clarity. The applied pulse sequences for **c** and **d** are pulse strings with each duration of 10 ms and scanning magnitude between the maximum $\pm J_x$, and all R_H data point are measured 2 seconds after the application of each pulse. For the AHE detection of R_H in **b-d**, a small +*x* directed d.c. current with fixed magnitude of 100 μA is used as the current source. **e,** Evolution of J_x^{th} and J_x^f with the increasing $\mu_0 H_x$. **f,** $\mu_0 H_x$ dependence of the current controllable region ΔJ_x (= J_x^{th} - J_x^f, the blue circles) and the current controllable proportion $\Delta J_x / J_x^f$ (the green spots). **g,** Maximum anomalous Hall resistance R_H^{max} as a function of $\mu_0 H_x$.

Table of Contents (ToC)

ToC text: A binary perpendicular ferromagnet was found to exhibit multi-state current-driven magnetization switching behaviors tunable by in-plane external magnetic fields. Based on this phenomenon, field-free magnetization-represented synaptic plasticity was implemented in a Pt/perpendicular-FM1/Ta/in-plane-FM2 structure with a built-in effective in-plane coupling field. This result paves an application pathway towards employing spintronic devices as synaptic emulators for neuromorphic computing.

ToC figure: (110 mm × 20 mm)

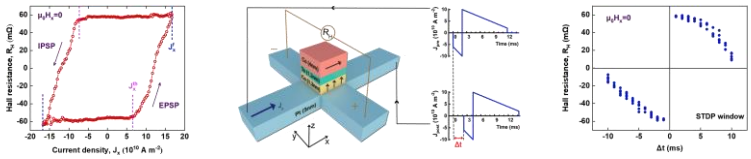

ToC keyword: Spintronic synapse

Supporting Information

Tuning a Binary Ferromagnet into a Multi-state Synapse with Spin-orbit Torque Induced Plasticity

*Yi Cao, Andrew Rushforth, Yu Sheng, Houzhi Zheng, and Kaiyou Wang**

Dr. Y. Cao, Y. Sheng, Prof. H. Zheng, Prof. K. Wang
State Key Laboratory for Superlattices and Microstructures
Institute of Semiconductors
Chinese Academy of Sciences
Beijing 100083, China
E-mail: kywang@semi.ac.cn

Prof. A. Rushforth
School of Physics and Astronomy
University of Nottingham
Nottingham NG7 2RD, United Kingdom

Prof. H. Zheng, Prof. K. Wang
Center of Materials Science and Optoelectronic Engineering
University of Chinese Academy of Science
Beijing 100049, China

Prof. K. Wang
Center for Excellence in Topological Quantum Computation
University of Chinese Academy of Science
Beijing 100049, China

* Corresponding e-mail: kywang@semi.ac.cn

Contents:

Note 1. Magnetic properties of the Pt/FM1/Ta/FM2 sample

As shown in Supplementary Figure S1, the PMA in FM1 and the IMA in FM2 are confirmed by the parallelogram-shaped out-of-plane and in-plane hysteresis loops, respectively. While the out-of-plane loop shows a well-defined rectangular shape, the in-plane loop shows a smaller zero-field Kerr rotation signal than its full value, indicating an unsaturated remanence in the IMA FM2 layer. This leads to a partial field-free SOT-induced switching of the PMA FM1 layer since the assisting in-plane coupling field from the FM2 layer acts only on a part of the FM1 layer. This is confirmed by the SOT-induced switching loops under small in-plane external magnetic field (for example, 20mT) as shown in the Supplementary Figure S4, where almost identical Hall resistance changes compared with the full Hall resistance loop in manuscript Figure 1b are obtained because the magnetization of FM2 remains saturated under the in-plane external field. While the unsaturated in-plane Co (4 nm) layer as the FM2 layer is adequate for us to show the concept of the demonstrated multi-state Pt/FM1/Ta/FM2 spintronic synapse in this work, other FM2 layers with full remanence and thereby full range field-free SOT-induced switching could be engineered by adopting in-plane uniaxial magnetic anisotropy materials, or by introducing an additional in-plane shape anisotropy or a particular strain along the current direction.[51-54]

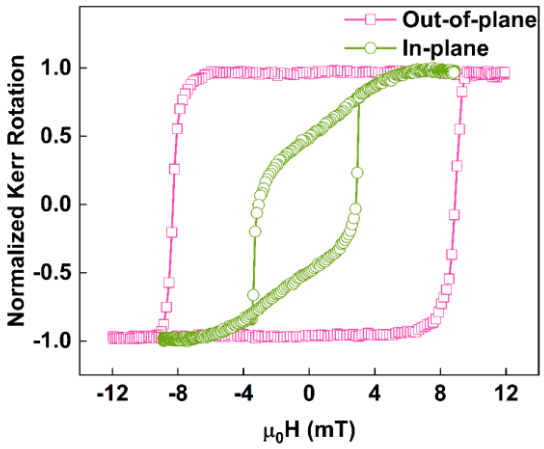

Supplementary Figure S1 | Magneto-optic Kerr loops for the pillar of the Pt/FM1/Ta/FM2 double magnetic layered device. The pink squares and the green circles correspond to Kerr loops measured out-of-plane and in-plane, respectively.

Note 2. Nonvolatility of the intermediate magnetization states

The R_H - *time* relations of the Pt/FM1/Ta/FM2 device were measured right after it was set to arbitrary R_H values by current pulses. The typical results are shown in Supplementary Figure S2a, where arbitrary intermediate R_H values (black squares and red circles) exhibited good nonvolatility within the measurement time scale (1800 seconds). Meanwhile, the magnetization states for negative saturated R_H values (blue triangles) showed a slight relaxation process within the beginning 200 seconds. As shown in Supplementary Figure S2b, an additional measurement with longer time scale (18000 seconds) was performed, suggesting that the negative maximum R_H state also became nonvolatile after the relaxation. Repeated measurements for negative as well as positive saturated R_H values often showed similar relaxation phenomenon with varying relaxation time, magnitude, and even directions, whereas repeated measurements for various intermediate R_H values are found to be much more stable without obvious relaxation process. Following these results, we claim the nonvolatility of the intermediate magnetization states in our Pt/FM1/Ta/FM2 device cautiously as "nonvolatile within our measurement time scale after an initial small relaxation".

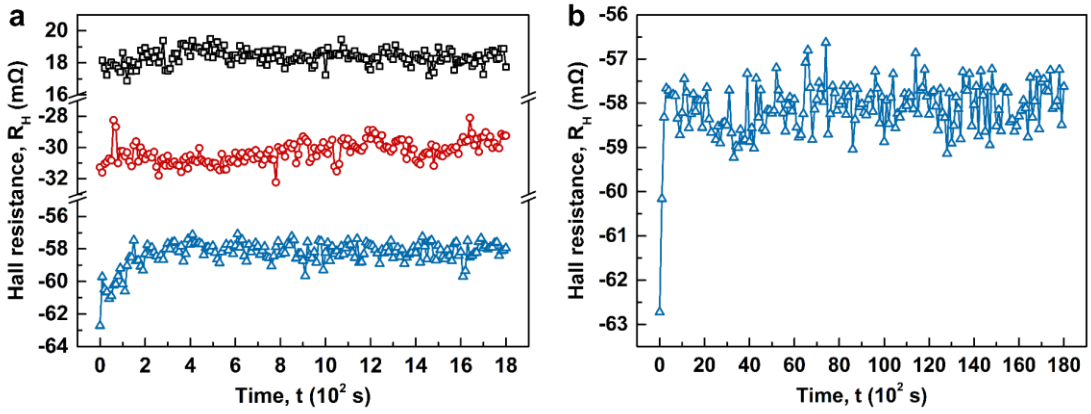

Supplementary Figure S2 | Time variation of the Hall resistance in the Pt/FM1/Ta/FM2 device. a, Time variation of arbitrary positive intermediate (black squares), arbitrary negative intermediate (red circles), and a negative saturated (blue triangles) R_H values. Each sequence of measurement started 500 ms after the device was set to arbitrary R_H values by a proper current pulse (i.e. the initial data for t = 0 was detected 500 ms after the pulse application) and lasted for 1800 seconds, during which time the Hall resistance were detected every 10 seconds. **b**, R_H - *time* relation for the negative saturated R_H value (blue triangle data in **a**) with longer time scale. The measurement lasted for 18000 seconds and the data were shown every 100 seconds.

Note 3. Adjustable current-induced magnetic switching direction by reversing the pre-magnetization of FM2

After applying a field of 20 mT along the -x-direction, the magnetization of FM2 was expected to be reversed. Then we removed the external field and measured the pulse current induced R_H-J_x loop using the same pulse sequence that was used for Manuscript Figure 1c. The result is shown in Supplementary Figure S3, where a clockwise R_H-J_x loop indicates an x-directed interlayer exchange coupling field generated by the FM2 layer that was magnetized along -x-direction. Note that the EPSP and IPSP here are induced by the negative and the positive increasing J_x, respectively, which are opposite to the EPSP and IPSP in Manuscript Figure 1c. In this way, the direction of synaptic plasticity in our device can be simply adjusted by controlling the magnetization of the FM2 layer.

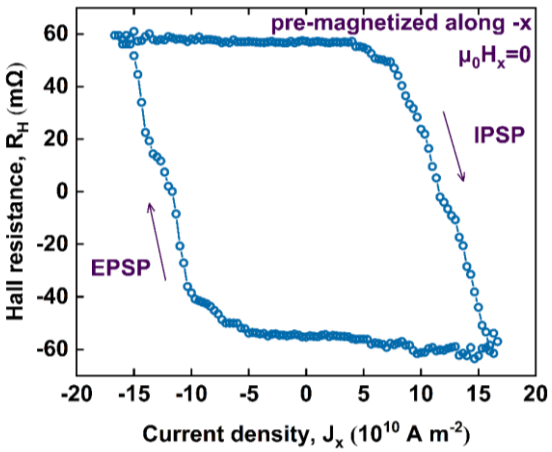

Supplementary Figure S3 | Magnetic-field-free R_H-J_x loop for the Pt/FM1/Ta/FM2 double magnetic layered device where the magnetization of FM2 layer is along -*x*-direction. An -*x* directed external magnetic field of 20 mT is applied to pre-magnetize the FM2 layer. Then the in-plane external field is removed. A sequence of pulses with scanning magnitude from -16.67×10^{10} A m^{-2} to 16.67×10^{10} A m^{-2} and then back to -16.67×10^{10} A m^{-2} is applied. The duration of every pulse is 10 ms, and every R_H is measured 2 seconds after the application of each pulse. For the AHE detection of R_H, a small +*x* directed d.c. current with fixed magnitude of 100 μA is used as the current source.

Note 4. Magnitude of the interlayer exchange coupling field ($\mu_0 H_x^c$)

It is widely known that the magnitude and sign of interlayer exchange coupling oscillates with the thickness of the spacer layer between two magnetic layers.[55] In our Pt/FM1/Ta/FM2 system with the optimized stack structure of Ta(0.5)/Pt(3)/Co(1.3)/Ta(1.2)/Co(4)/AlO_x(2) (thickness in nm), the interlayer exchange coupling field ($\mu_0 H_x^c$) acting on the Co(1.3 nm) free layer coming from the upper Co(4 nm) fixed layer via the Ta spacer can be obtained from Supplementary Figure S4, where the sense of rotation of the R_H-J_x loops is reversed at $\mu_0 H_x \approx 180$ mT. Particularly, as $\mu_0 H_x$ increases from low value to 180 mT, the R_H-J_x loops are anticlockwise; When $\mu_0 H_x > 180$ mT, the R_H-J_x loops become clockwise because the $\mu_0 H_x^c$ is overcome by the $\mu_0 H_x$, which results in a net magnetic field along +*x*-direction. Therefore, we have an antiferromagnetic interlayer exchange coupling with $\mu_0 H_x^c \approx -180$ mT.

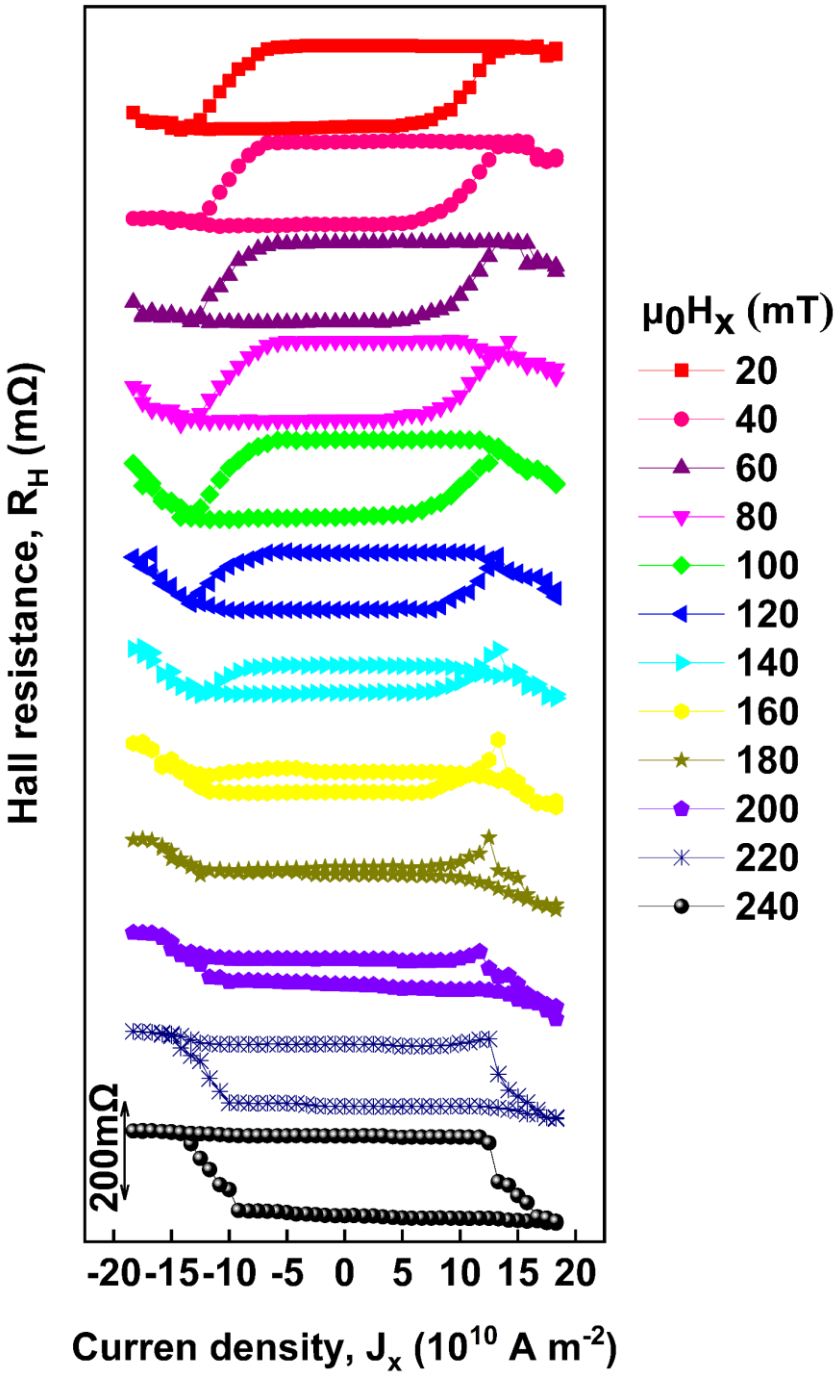

Supplementary Figure S4 | Pulse current-driven R_H-J_x SOT switching loops for the Pt/FM1/Ta/FM2 double magnetic layered device. Loops with various $\mu_0 H_x$ from 20 mT to 240 mT are shifted vertically for clarity. The magnetization of FM2 Co(4 nm) layer is pre-magnetized along the +*x*-direction. The applied pulse sequence is a pulse string with each duration of 10 ms and scanning magnitude between the maximum $\pm J_x$, and all R_H data point are measured 2 seconds after the application of each pulse. For the AHE detection of R_H, a small +*x* directed DC current with fixed magnitude of 100 μA is used as the current source.

Note 5. Simulations of STDP resulted by overlapped spikes

To simulate the STDP window by the overlapped spikes, we firstly fit the function $R_H^{single\ pulse}(J_x)$ of R_H versus single pulse's J_x from the experimental data in Manuscript Figure 2b. Then the amplitude of pre- and post-spikes (J_{pre} and J_{post}) can be presented as time t-dependent piecewise functions. Because the post-spike shares the same waveform with the pre-spike but comes from the contrary direction with a time delay of Δt, thus we can overlap the pre- and post-spikes and obtain the amplitude of overlapped spikes (J_{ovlp}) as a function of Δt by $J_{ovlp}(\Delta t) = J_{pre}(t) - J_{post}(t, \Delta t)$. Finally, the STDP window (in form of a R_H-Δt function) can be obtained by plugging the J_{ovlp}-Δt function into the $R_H^{single\ pulse}$-J_x function, which can be represented as $R_H^{STDP}(\Delta t) = R_H^{single\ pulse}\left(J_{ovlp}(\Delta t)\right)$.

Using the experimental waveform function of E0, E1 and E2 in Manuscript Figure 2c and 2e, the simulated STDP windows, as shown in Supplementary Figure S5b, are very similar to that of the experimental results. If we change the decay part of the spike waveform to an exponential function, as shown in Supplementary Figure S5c, the exponential STDP window postulated by Bi and Poo can also be obtained, as shown in Supplementary Figure S5d.[45] Thus, by modifying the spike waveform, different STDP windows can be obtained, which could enable our synaptic device with the capabilities of different learning rules.[48]

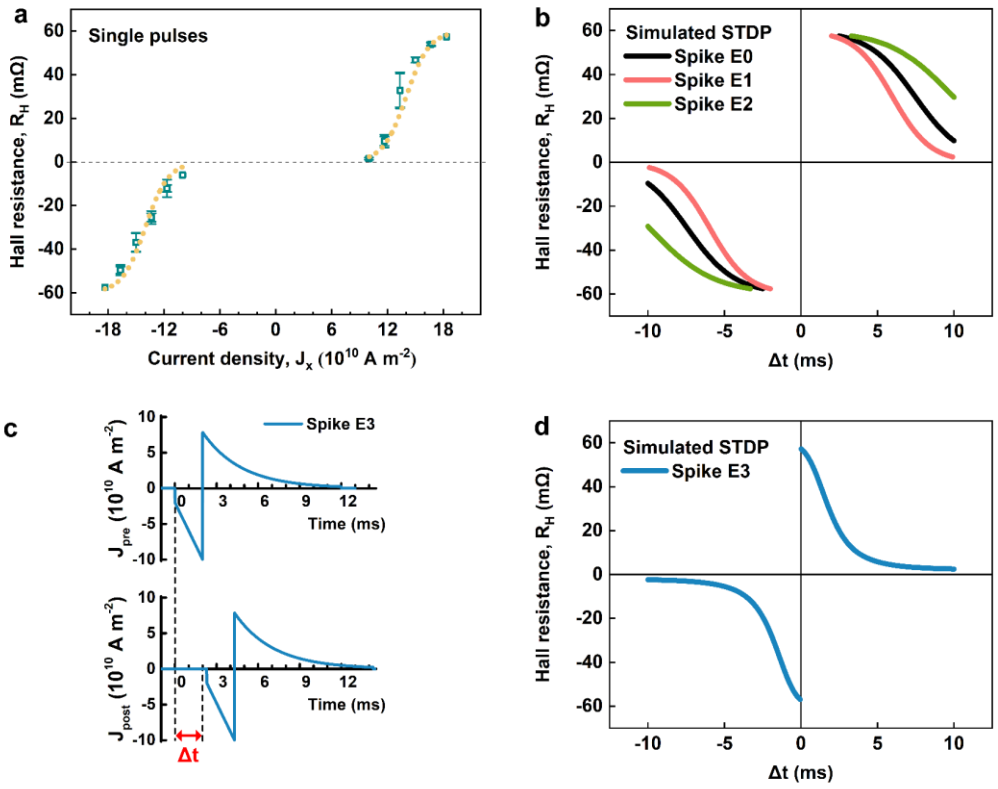

Supplementary Figure S5 | Simulations of STDP resulting from overlapped spikes. a, Fittings (yellow dotted line) of the R_H changes by single pulses in Manuscript Figure 2b. **b,** simulated STDP windows for Spike E0, E1, and E2. **c,** Spike waveform with exponentially decaying amplitude (Spike Exp). **d,** simulated STDP window for Spike Exp.

Note 6. The magnetization reversal mechanism

6.1 Domain wall motion images

We directly imaged the domain patterns of the Pt/FM1/Ta device with 20 μm-wide squared pillar by magneto-optic Kerr mapping. During the measurements, an external in-plane field of $\mu_0 H_x$ = 120 mT was applied, where the parallelogram-like current-induced magnetic switching loop in the Pt/FM1/Ta reference sample is similar to that of the Pt/FM1/Ta/FM2 system. Supplementary Figure S6a shows the current-driven R_H-J_x loop, where a sequence of pulses with scanning magnitude from 4.5×10^{10} A m^{-2} to -4.5×10^{10} A m^{-2} and then back to 4.5×10^{10} A m^{-2} was applied. The duration of each pulse was 10 ms and the interval between neighboring pulses was 2 seconds, within which time more than one Kerr image could be taken. The

corresponding Kerr microscope images of the pillar during its down-to-up and up-to-down m_z switching processes are shown in Supplementary Figures S6b1-b8 and Supplementary Figures S6c1-c8, respectively. At the beginning of the down-to-up switching process with threshold pulse magnitude $J_x = -2\times10^{10}$ A m^{-2}, nucleation of a small domain is found to appear at the edge of the pillar, as shown by the dark area (up m_z) in Supplementary Figure S6b1. The domain wall propagates across the pillar with the increasing negative J_x (Supplementary Figures S6b2-b7), and finally fills up the pillar area at a finishing switching current $J_x = -3.75\times10^{10}$ A m^{-2} (Supplementary Figure S6b8). It is similar for the up-to-down switching process, where nucleation of two or three domains form at the current-entrance edge (bright areas in Supplementary Figure S6c1) before they enlarge and merge as they propagate across the pillar along the $+x$-direction as J_x increases (Supplementary Figures S6c2-c9). Regardless of the nucleation numbers, the switching process in our Pt/FM1/Ta structure with $\mu_0 H_x$ = 120 mT is thus dominated by domain wall propagation. The multistate behavior observed in the field driven (Manuscript Figure 1b) and current driven (Manuscript Figure 1c) cases is consistent with domain wall motion across multiple pinning sites. Thus, the underlying mechanism for the multi-state magnetization reversal in our Pt/FM1/Ta structure with in-plane external field, and therefore the Pt/FM1/Ta/FM2 structure with inherent antiferromagnetic coupling field, should be ascribed to a pulse magnitude-dependent domain wall motion process. When there is sufficient pinning, the domain wall positions will be stable and thereby make our device a nonvolatile multi-state memory.[56,57]

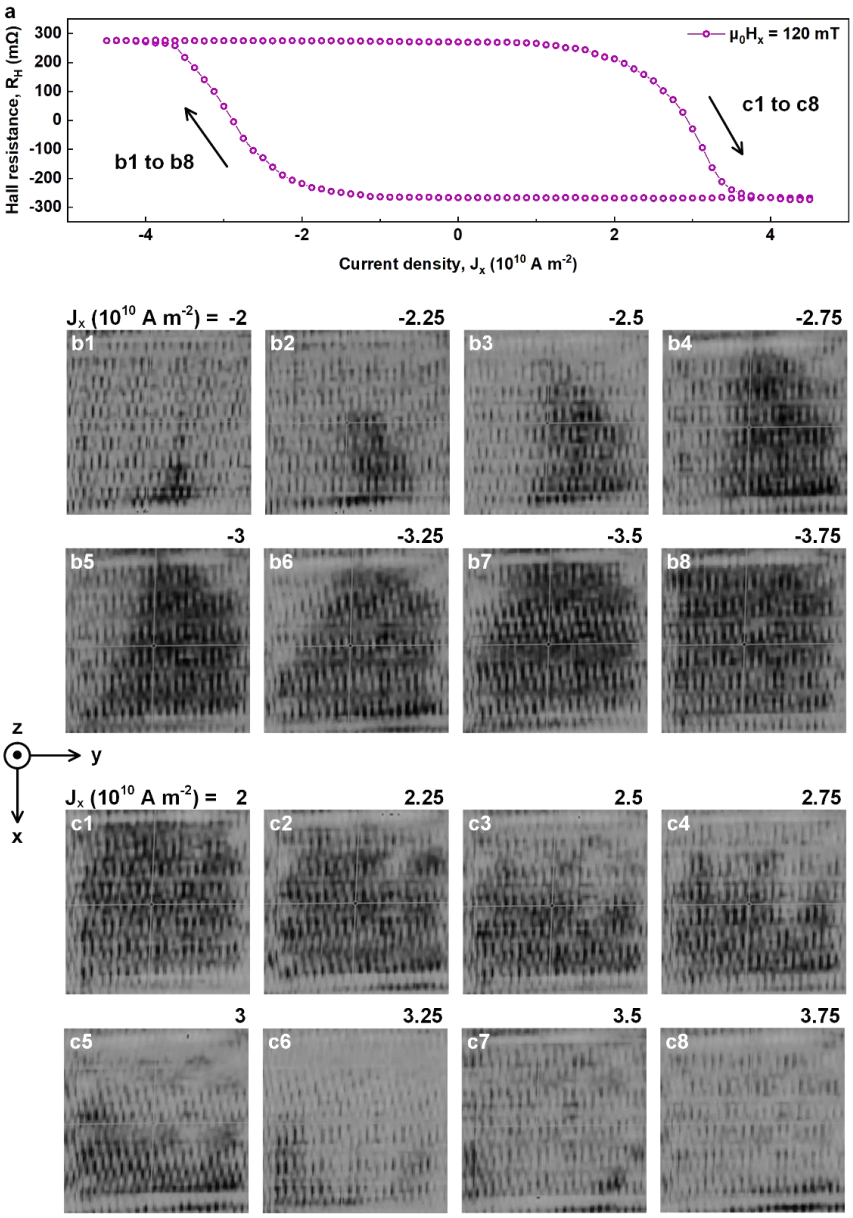

Supplementary Figure S6 **| Current-driven domain wall motion in a 20 µm-wide Pt/FM1/Ta squared pillar with $\mu_0 H_x$ = 120 mT. a,** Pulse current-driven R_H-J_x loop with external magnetic field $\mu_0 H_x$ = 120 mT. The sequence of pulses each with duration of 10 ms and scanning magnitude from 4.5×10^{10} A m^{-2} to -4.5×10^{10} A m^{-2} and then back to 4.5×10^{10} A m^{-2} is applied, and all R_H data points are measured 2 seconds after the application of each pulse. **b1-b8,** Kerr microscope images during the down-to-up switching process from negative R_H to positive R_H. **c1-c8,** Kerr microscope images during the up-to-down switching process from positive R_H to negative R_H. Bright and dark contrast corresponds to down and up m_z directions, respectively.

6.2 Determination of the DMI field

Current induced domain wall motion in ferromagnetic metal (FM)/ heavy metal (HM) systems with perpendicular magnetic anisotropy is understood to arise from a combination of the spin transfer torque (STT) mechanism due to electrons flowing within the ferromagnetic material, and the anti-damping (also known as Slonczewski-like) torque due to the spin accumulation at the heavy metal/ferromagnet interface, generated by the spin Hall effect (SHE) in the heavy metal.[58] We refer to the latter mechanism as SHE-STT to distinguish it from the former conventional STT mechanism. The Rashba effect, arising due to an asymmetric layer structure, can give rise to field-like and Slonczewski-like torques.[41,59,60] Finally, the Dzyaloshinskii-Moriya interaction (DMI) arising at the heavy metal/ferromagnet interface stabilises the Néel domain wall configuration with the same preferred chirality for up/down and down/up domain wall configurations.[28] Typically, the SHE-STT provides the dominant torque, leading to the motion of up/down and down/up domain walls in the same direction when the DMI ensures that both domain walls possess the same chirality. This property prevents the magnetization reversal of devices by SHE-STT unless the DMI is compensated by an external effective magnetic field so that up/down and down/up domain walls possess opposite chirality and can be driven in opposite directions by the current.

The magnitude of the field arising due to the DMI can be determined by measuring the d.c. current J_x induced perpendicular effective field ($\mu_0 H_z^{eff}$) as a function of the applied in-plane bias magnetic field ($\mu_0 H_x$) until $\mu_0 H_x$ approaches the DMI field. $\mu_0 H_z^{eff}$ can be obtained by measuring the magnetic hysteresis loops under a particular J_x and $\mu_0 H_x$, where the loop for a positive (negative) $\mu_0 H_x$ will offset leftward (rightward) with a value of $\mu_0 H_z^{eff}$ from the loop for $\mu_0 H_x = 0$.[61] Following this method, we measured the out-of-plane MOKE loops at the pillar of our 6 μm-wide Pt/FM1/Ta device with a fixed d.c. $J_x = 1.39\times10^{10}$ A m^{-2} and various $\mu_0 H_x$, as shown in Supplementary Figure S7a. The obtained $\mu_0 H_z^{eff}$ as a function of the $\mu_0 H_x$ is shown in Supplementary Figure S7b. From this we can estimate that the strength of the field due to the DMI in our devices is approximately 40 mT.

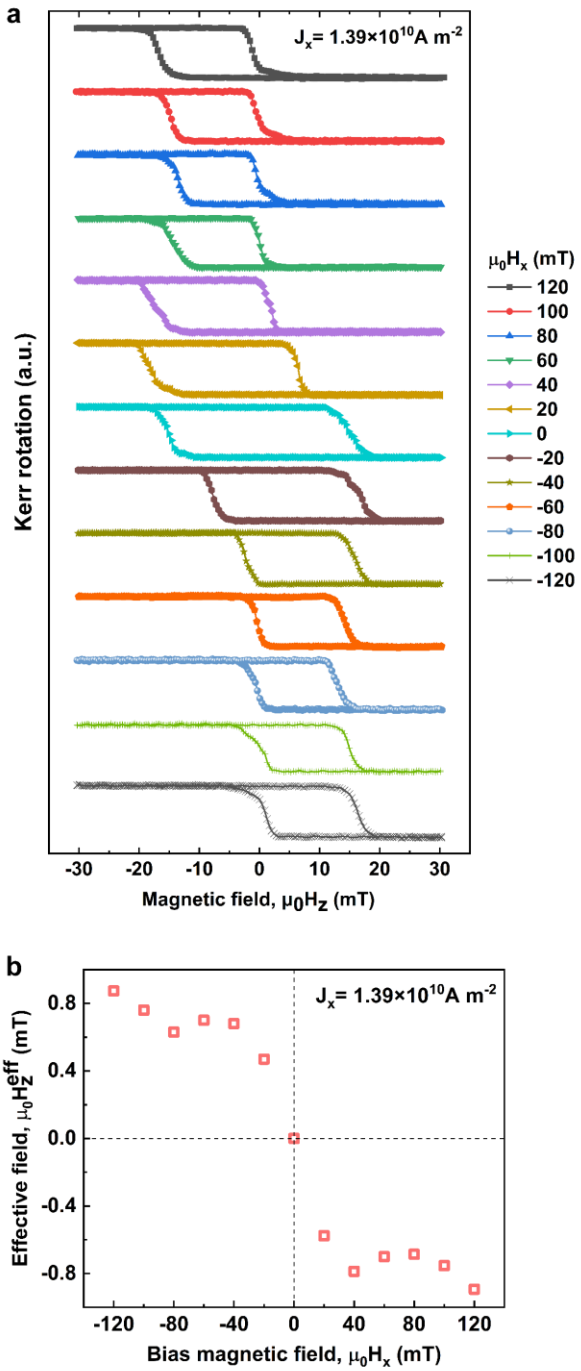

Supplementary Figure S7 | D.C. current J_x induced perpendicular effective field $\mu_0H_z^{eff}$ for the Pt/FM1/Ta reference device under various in-plane bias magnetic field μ_0H_x. The pillar width of the device is 6 μm. **a**, Out-of-plane MOKE loops measured under a fixed d.c. current with J_x = 1.39×10^{10} A m^{-2} and various in-plane bias magnetic field μ_0H_x. Loops are shifted vertically for clarity. The relative horizontal offset between each loop and the loop for μ_0H_x = 0 can be read as the current induced perpendicular effective field $\mu_0H_z^{eff}$, whose evolution with the μ_0H_x is plotted in **b**.

6.3 Numerical calculations

We modelled the motion of a domain wall using the rigid one-dimensional model modified to include the effects of STT, SHE-STT and DMI. The model has been shown to provide a good qualitative description of domain wall motion along nanowire strips with perpendicular magnetic anisotropy, including the effects of the SHE-STT and DMI.[50,62-64] The model describes the domain wall behaviour through two coupled Equations (S1) and (S2) based on the position X along the nanowire and the azimuthal angle ϕ.

$$(1+\alpha^2)\frac{dX}{dt} = \alpha\gamma\Delta H_Z + (1+\alpha\beta)b_J + \frac{\alpha\gamma\Delta\pi}{2}H_{SHE}\cos(\phi) + \frac{\gamma\Delta\pi}{2}H_{DMI}\sin(\phi) + \frac{\gamma\Delta\pi}{2}H_x\sin(\phi) \quad \text{(S1)}$$

$$(1+\alpha^2)\frac{d\phi}{dt} = \gamma H_Z + (\beta-\alpha)\frac{b_J}{\Delta} + \frac{\gamma\pi}{2}H_{SHE}\cos(\phi) - \frac{\alpha\gamma\pi}{2}H_{DMI}\sin(\phi) - \frac{\alpha\gamma\pi}{2}H_x\sin(\phi) \quad \text{(S2)}$$

Where the parameters, with values appropriate for the studied Pt/Co/Ta trilayer system include the Gilbert damping term, α = 0.2, the gyromagnetic ratio, γ = 2.21×10^5 m A^{-1} s^{-1}, the domain wall width, Δ = 10 nm, and the STT non-adiabaticity parameter, β = 0. STT is represented by $b_J = \mu_B P j / e M_S$, where j is the current density, P = 0.5 is the spin polarisation, M_S = 1.4×10^6 A m^{-1} is the magnetization of the Co layer, μ_B is the Bohr magneton and e = -1.6×10^{-19} C is the charge on the electron. The effective fields due to the SHE and DMI are $H_{SHE} = \hbar\theta_{SH} j / 2\mu_0 e M_S t$, and H_{DMI}, in the directions transverse (y) and parallel (x) to the current direction respectively. θ_{SH} = 0.1 is the spin Hall angle and t = 1.3 nm is the Co layer thickness. H_x is the effective magnetic field in the plane of the layer in the x-direction. We set H_{DMI} = 0 for the calculations because it is clear that H_{DMI} only acts as an offset to H_x.

We modelled the effects of pinning as a spatially dependent field component in the z-direction given by $H_Z = B\frac{\partial V}{\partial X}$, where B represents the strength of the pinning potential and $V = sin^2(\pi X/\xi)$ with ξ = 30 nm. Thermal effects were modelled as an uncorrelated Gaussian distributed stochastic fluctuation of H_Z. Each calculation was averaged over five such random distributions.

Supplementary Figure S8a shows the calculated domain wall velocity, v, versus the current density j, for various $\mu_0 H_x$, when the pinning potential is relatively weak ($B = 8\times10^{-29}$ J). As current increases, the velocity increases initially, before saturating at some value which is dependent on $\mu_0 H_x$. This is because the SHE-STT term tends to drive the azimuthal angle, ϕ, towards some equilibrium value between the Bloch and Néel configurations, at which point $d\phi/dt = 0$ and a constant velocity is maintained which depends on the balance between the terms involving H_{SHE} and H_x. For larger $\mu_0 H_x$, the velocity is higher at any value of current because the applied field acts against the tendency for ϕ to rotate towards the Bloch configuration, thereby allowing the SHE-STT to make a more significant contribution to the overall velocity. In this regime, the pinning potential has a relatively weak effect on the domain wall motion.

Supplementary Figure S8b shows the calculated velocity versus current for a relatively strong pinning potential ($B = 8\times10^{-28}$ J). Now the pinning potential has a more significant effect on the domain wall motion. For low current densities the velocity is suppressed because the pinning potential prevents uniform domain wall motion. At higher current densities the domain wall motion becomes less stochastic and the velocity increases significantly with increasing current density, until it saturates in a similar manner to that observed for the weak pinning potential.

The numerical simulations give a good qualitative understanding of the phenomena observed experimentally. As with other results from using the 1-dimensional model a full quantitative agreement is not expected.[50,62,63]

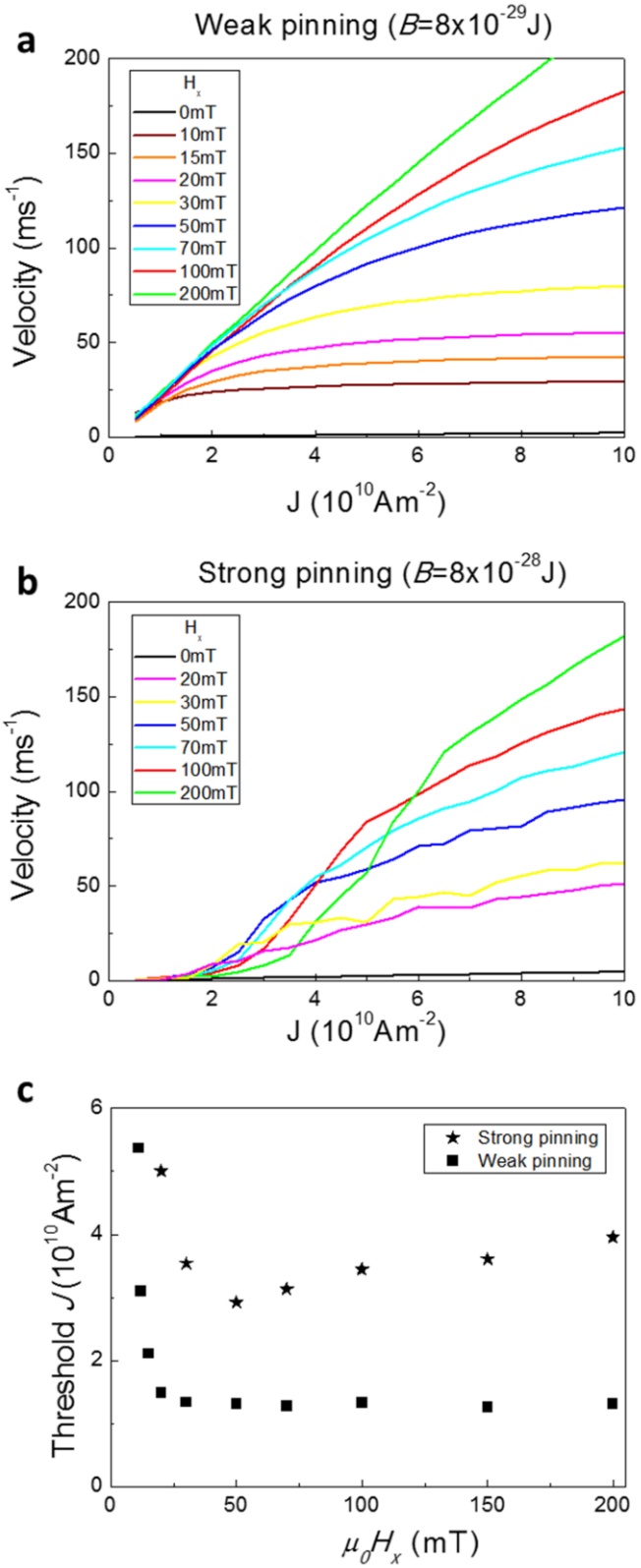

Supplementary Figure S8 | Calculated domain wall velocity, plotted against current density, *j*, for various in-plane magnetic field $\mu_0 H_x$. Calculated velocity for **a**, weak and **b**, strong pinning potentials. **c,** the calculated threshold current density versus $\mu_0 H_x$ for the weak and strong pinning regimes.

6.4 Discussions of the broadened magnetization reversal process

At low current densities, where domain wall motion is stochastic, increasing $\mu_0 H_x$ decreases the importance of the terms involving H_{SHE} relative to those involving H_x in Equations (S1) and (S2), and ϕ remains close to the Néel configuration i.e. the SHE-STT term does not drive ϕ significantly away from $\phi = 0$. Domain wall motion can only proceed by stochastic fluctuations of ϕ, that are large enough to allow the last term in Equation (S1) to drive the domain wall motion across the pinning potential landscape. Increasing $\mu_0 H_x$ supresses the fluctuations in ϕ and therefore reduces the average domain wall velocity in this regime.

At high current densities, the opposite trend is observed. Here, H_{SHE} is significantly larger than H_x and is the dominant term in determining the domain wall velocity. As in the case with weak pinning potential, increasing $\mu_0 H_x$ causes the equilibrium value of ϕ to be closer to the Néel configuration, thereby increasing the contribution of the SHE-STT term to the domain wall velocity. Consequently, at high current densities, increasing $\mu_0 H_x$ causes the domain wall velocity to increase.

At intermediate current densities there is a transition between the regimes described above. For low $\mu_0 H_x$, increasing $\mu_0 H_x$ causes domain wall velocity to increase, whereas for higher $\mu_0 H_x$, the opposite trend is observed. This intermediate regime gives a good qualitative agreement with our experimental observations. We define a threshold domain wall velocity that is necessary in order to observe switching of the magnetization (in this case we choose $v = 30$ m s^{-1}, but the absolute value is not too important because the model is expected to give only qualitative understanding) and we plot the current density at which that velocity is reached as a function of $\mu_0 H_x$ in the weak and strong pinning regimes. As shown in Supplementary Figure S8c, the threshold current density for the weak pinning regime decreases with increasing $\mu_0 H_x$ in a manner similar to the experimental J_x^{th}, while the threshold current density for the strong pinning regime initially decreases with increasing $\mu_0 H_x$ before increasing for further increases in $\mu_0 H_x$ in a manner similar to the experimental J_x^f. This suggests that there is a distribution of strong and weak pinning sites in our device and that the onset of the magnetization reversal at J_x^{th} occurs when the current drives the domain wall

across weaker pinning sites, while the magnetization reversal completes at values of J_x^f sufficiently large to drive the domain wall across the stronger pinning sites. The different efficiencies of the spin-orbit torque in driving domain wall motion in the strong and weak pinning regimes leads to the broadening of the magnetic reversal transition as $\mu_0 H_x$ is increased.

The magnetic field applied in the plane will also tilt the magnetization in the regions of up and down pointing domains with the effect of reducing the magnitude of the *z*-component of the magnetization. This effect is not captured within the 1-dimensional domain wall model, so the possible effect on the domain wall velocity is not clear. It may account for the decrease of J_x^f at the highest values of $\mu_0 H_x$. It is likely to be responsible for the observed reduction of the magnitude of the change of R_H when the magnetization switches at high values of $\mu_0 H_x$.

Finally, we note that for current to flow within the FM Co layer in the pillars, it must first enter the region via the Pt layer. Therefore, the current density in the Pt will be largest at the edges where it enters or leaves the region of the pillar. The SHE-STT will be largest in these regions, which may explain why the domain walls observed in Supplementary Figure S6 nucleate at one edge of the pillar and propagate towards the opposite end. The chirality of the domain walls will be the same in the two sets of images in Supplementary Figures S6b1-b8 and S6c1-c8, which would be consistent with a small DMI field of 40mT and also the direction of the internal magnetization in the domain wall being aligned with the external magnetic field.

Note 7. Simulations of STDP under different magnitude of interlayer exchange coupling

According to Manuscript Figure 3, all the J_x^{th}, the J_x^f, and the ΔJ_x of the Pt/FM1/Ta sample change remarkably with the in-plane external field. Hence it is obvious that the magnitude of the interlayer exchange coupling field in the Pt/FM1/Ta/FM2 device would affect the switching parameters significantly, including the function of R_H versus single pulse's J_x in Manuscript Figure 2b.

Here we set two different functions of R_H versus single pulse's J_x, as shown in

Supplementary Figure S9a, for two different supposed coupling magnitudes (C1 and C2). Then we use the same exponentially decaying spike waveform function E3 in Supplementary Figure S5c to simulate the R_H-Δt functions for C1 and C2, respectively, and obtained two different STDP windows with distinctive decay slopes as a function of the $|\Delta t|$, as shown in Supplementary Figure S9b. This simulation shows that the plasticity of our Pt/FM1/Ta/FM2 can be efficiently controlled by means of modulating the magnitude of its interlayer exchange coupling field, which would bring more versatile computing capabilities in addition to the spike-waveform-dependent STDP window forms.

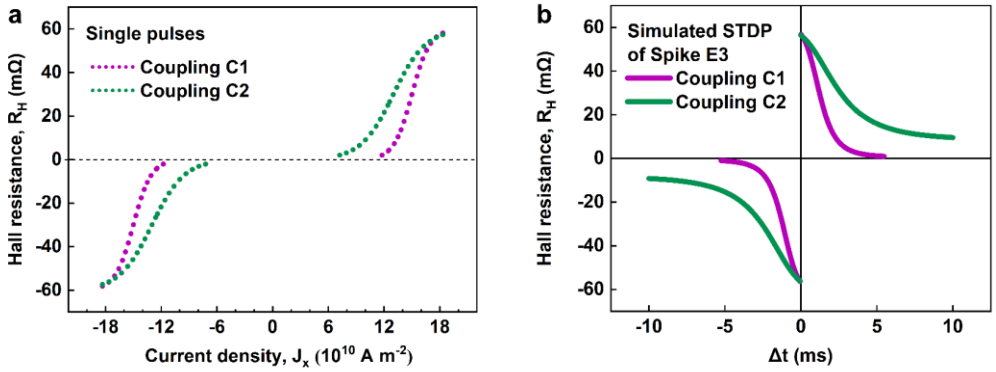

Supplementary Figure S9 | Simulations of STDP under different functions of R_H versus single pulse's J_x. a, The different given functions of R_H versus single pulse's J_x (for two corresponding supposed coupling magnitudes, C1 and C2, respectively). **b,** Simulated STDP windows for C1 and C2 with spike waveform in Supplementary Figure S5d (Spike Exp).

References

51. A. T. Hindmarch, A. W. Rushforth, R. P. Campion, C. H. Marrows, B. L. Gallagher, *Phys. Rev. B* **2011**, *83*, 212404.
52. R. P. Cowburn, *J. Phys. D: Appl. Phys.* **2000**, *33*, R1-R16.
53. H. Zhang, Y. Li. M. Yang, B. Zhang, G. Yang, S. Wang, K. Wang, *Chin. Phys. B* **2015**, *24*, 077501.
54. B. Zhang, K. Meng, M. Yang, K. W. Edmonds, H. Zhang, K. Cai, Y. Sheng, N. Zhang, Y. Ji, J. Zhao, H. Zheng, K. Wang, *Sci. Rep.* **2016**, *6*, 28458.
55. S. S. P. Parkin, N. More, K. P. Roche, *Phys. Rev. Lett.* **1990**, *64*, 2304.
56. K. Y. Wang, A. C. Irvine, J. Wunderlich, K. W. Edmonds, A. W. Rushforth, R. P. Campion, C. T. Foxon, D. A. Williams, B. L. Gallagher, *New J. Phys.* **2008**, *10* 085007.
57. S. S. P. Parking, M. Hayashi, L. Thomas, *Science* **2008**, *320*, 190.
58. A. V. Khvalkovskiy, V. Cros, D. Apalkov, V. Nikitin, M. Krounbi, K. A. Zvezdin, A. Anane, J. Grollier, A. Fert, *Phys. Rev. B* **2013**, *87*, 020402(R).
59. I. M. Miron, T. Moore, H. Szambolics, L. D. Buda-Prejbeanu, S. Auffret, B. Rodmacq, S. Pizzini, J. Vogel, M. Bonfim, A. Schuhl, G. Gaudin, *Nat. Mater.* **2011**, *10*, 419.
60. X. Wang, A. Manchon, *Phys. Rev. Lett.* **2012**, *108*, 117201.
61. C. F. Pai, M. Mann, A. J. Tan, G. S. Beach, *Phys. Rev. B* **2016**, *93*, 144409.
62. S. Emori, U. Bauer, S. M. Ahn, E. Martinez, G. S. D. Beach, *Nat. Mater.* **2013**, *12*, 611.
63. K. S. Ryu, L. Thomas, S. H. Yang, S. Parkin, *Nat. Nanotech.* **2013**, *8*, 527.
64. E. Martinez, *J. Phys.: Condens. Matter.* **2011**, *24*, 024206.